“Finite element simulations of sill intrusion during tectonic loading”

S.P.A. Gill and R.J. Walker

Finite element simulations of sill intrusion during tectonic loading

S.P.A. Gill[1] and R.J. Walker [2]

[1]University of Leicester, Department of Engineering, University Road, Leicester, LE1 7RH, UK.
[2]University of Leicester, School of Geography, Geology, and the Environment, University Road, Leicester, LE1 7RH, UK.

*Corresponding author: rich.walker@le.ac.uk

KEY POINTS

- We investigate saucer-shaped sill growth using finite element simulation, with comparison to natural and modelled sills.
- Geometries of sills emplaced during mild horizontal shortening closely match the profiles of natural saucer-shaped sills.
- Tip stresses generated by overburden bending and the tectonic stress, compete to respectively steepen or flatten the sill.

ABSTRACT

Igneous sills are common features in volcanically and tectonically active regions, acting as nascent magma storage systems, or potentially feeding eruptions at large lateral distances from the magma source. Sills that reach a critical radius length, r_c, relative to their initial depth, H, interact with Earth's surface, leading to mild discordant growth at angle θ typically $< 10°$ forming saucer-shaped sills; it is common for natural sills that $r_c > 3H$. Most analogue and numerical models for sills produce saucer shapes where $\theta > 20°$ and $r_c < H$; they do not resemble natural sills. Here we use the finite element method to simulate sill intrusion in homogenous media subjected to an excess compressive tectonic horizontal stress, σ_r. Tests were conducted for a range of σ_r, ranging from no applied excess stress (lithostatic), and σ_r up to the magnitude of magma overpressure, P_o, used in the models (here 5 MPa). Sills emplaced where $\sigma_r = 0$, grow in the horizontal plane to $r_c \approx 1.5H$, before climbing towards the surface at $\theta \approx 25°$. Mild increases in σ_r resulted in an increase in r_c, and a decrease in θ. At higher σ_r, r_c relatively decreased and θ increased. Increasing the host shear-cohesion, C, does not affect θ under lithostatic conditions, but promotes a decrease in r_c; θ consistently decreased with increasing σ_r. The best correlation between simulated and natural sills is when $\sigma_r \approx P_o$. Saucer-shaped sill geometry reflects the additive stress components of the magma overpressure within the sill, and the tectonic stress. Magma overpressure produces the majority of stress driving propagation, generating a stress intensity due to the overpressure $K_p \propto P_o\sqrt{H}$. Sill growth is controlled by the locus of the maximum energy release rate, G, which is initially in-plane with the sill, but deflects to ~25° at r_c due to interaction between the sill and the free surface. This deflection is subdued by σ_r, which produces a stress intensity $K_r \propto \sigma_r\sqrt{h}$, where h is the vertical climb of the sill from H. Tectonic stress is a primary control on the geometry of saucer-shaped sills; host rock cohesion and elastic properties control the absolute magnitudes of tectonic loading required to affect a change in sill geometry.

PLAIN LANGUAGE SUMMARY

Horizontal magma pathways – sills – are a crucial part of volcanic plumbing systems, acting as potential feeder conduits to volcanic eruptions, and as magma storage systems. Saucer-shaped sills, which exhibit a flat inner region and inclined outer region, are a common type of magma pathway in the shallow crust. Models for saucer-shaped sills, both as physical analogue models, or numerical simulations, typically under-predict the length of the inner flat region, and over-predict the outer inclined region; models are typically too short and too steep. Here we use numerical simulation to investigate parameters that may control sill shape. We find that the dominant controls on sill shape are the competing effects of: (1) bending of the rocks above the sill, which promotes a transition to

inclined growth, typically at ~25°; and (2) plate tectonic shortening, which serves to decrease the angle of incline, towards 0° when the horizontal force is high. Increasing the applied horizontal tectonic force can produce sills that are up to five times longer in the inner region, before growing as inclined sills at ~5°. This matches very closely with observations of natural sills, indicating that tectonic forces are an important consideration in the growth of sills.

1. INTRODUCTION

Igneous sills have played a primary role in the formation of Earth's oceanic crust (Maclennan, 2018) and the growth of evolved continental crust (Jackson et al., 2019). Sills have been shown to represent an important part of the plumbing system in volcanically active regions (Amelung et al., 2000; Sigmundsson et al., 2010) and in ancient systems (Leat, 2008; Muirhead et al., 2014). Sills are common in association with horizontally-layered sedimentary rocks (e.g., in basin settings), and typically considered as initially flat-lying intrusions that are parallel to bedding, representative of extension (mode I) cracks. Sills that cut bedding are observed, at a range of scales (metre to kilometre), including: (1) gently transgressive sills inferred to relate to horizontal shortening (tectonic) strains, which accommodate mode I-II extensional-shear opening (Fig. 1; Walker, 2016; Walker et al., 2017; Stephens et al., 2017, 2018); and (2) saucer-shaped sills, defined by a broadly convex profile that consists of a flat inner region, with transgressive flanks (Fig. 1; Malthe-Sorenssen et al., 2004; Planke et al., 2005; Polteau et al., 2008; Hansen et al., 2011). In the latter case, the characteristic saucer shape is typically related to asymmetry in sill-tip stress during propagation, due to inflation-induced bending of the overburden (Malthe-Sorenssen et al., 2004; Galland et al., 2009). Other proposed mechanisms for saucer-shaped sill formation include the depth-dependent increase in Young's Modulus E (Hansen, 2015), or shear failure of the overburden (Haug et al., 2017,2018). Analogue models (Galland et al., 2009; Galland and Scheibert, 2013) and numerical simulations of sill growth (Chen et al., 2017) using isotropic host materials, have demonstrated that the saucer shape is a fundamental geometry.

Transition from the flat inner region to inclined outer region of natural saucer-shaped sills (e.g., Fig. 1) typically occurs at some critical radius length scale (r_c) relative to the initial depth of emplacement (H), typically where $r_c > 3H$ (Fig. 2). The incline section of natural sills typically rises at an angle $\theta < 30°$ (Fig. 1), which initiates at a low angle and increases in dip towards the extremities, defining a convex profile (Fig. 1 and 2). By contrast, and in general, most modelled saucer-shaped sills differ from natural sills in three critical ways: (1) $r_c \ll 3H$ (Galland et al., 2009); (2) $\theta \geq 30°$ (Haug et al., 2017); and (3) sill incline profiles are concave, with θ initially steep, before decreasing at distance from the sill centre (Malthe-Sorenssen et al., 2004; Galland et al., 2009; Haug et al., 2017,2018). In almost all cases, models for saucer-shaped sills are conducted in initially isotropic conditions, with the exception that the sill is typically seeded at some initial depth by a material interface (Galland et al., 2009) or crack (Bunger et al., 2008), or the sill already exists in the model. Initial stresses in the models are typically lithostatic ($P_L = \sigma_{xx} = \sigma_{yy} = \frac{\nu}{1-\nu}\sigma_{zz}$ where σ_{zz} is the vertical stress, $\sigma_{xx}$and σ_{yy} are the horizontal stresses, and ν is Poisson's ratio, the ratio of lateral to axial strain; $\sigma_{zz} = \rho_r g z$, where ρ_r is the rock density, g is the gravitational constant $9.81\ m/s^2$, and z is the depth), or hydrostatic (i.e. $\sigma_{xx} = \sigma_{yy} = \sigma_{zz}$ in which case $\nu = 0.5$, or the deviatoric stress has been removed via creep). Bunger et al. (2008) showed that the application of a radial compressive stress during analogue models in which $\sigma_{xx} = \sigma_{yy} > \sigma_{zz}$ reduced the effect of anisotropic stress ahead of the propagating tip, producing saucer-shaped sills with $30° > \theta > 5°$, more closely resembling natural saucer-shaped sills (Fig. 2). However, in general we note that for modelled sills (1) the critical sill radius r_c is too short, (2) θ is too high, and (3) the sill profiles are mostly concave (Fig. 2).

Here we use a finite element (FE) simulation to consider the effect of the magma pressure profile within sills, and of horizontal stress on sill dimensions, geometry, and emplacement mode. We show that the deviatoric horizontal stress ($\sigma_{xx} = \sigma_{yy} \neq \sigma_{zz}$) is important in controlling intrusion geometry, but also in controlling emplacement mode, causing a transition from extension to extensional-shear mode opening of the intrusion.

2. METHODS

2.1. The model

Three mutually dependent physical processes are involved in the sill intrusion process: (1) elastic deformation of the host rock, which varies as a function of the overburden tectonic stresses and the magma overpressure distribution within the sill; (2) fracture of the host rock; and (3) viscous flow of magma through the fracture. These are represented by partial differential equations which we solve here using the finite element (FE) method. An advantage of this method is that it is particularly well suited for solving strongly-coupled, globally-connected problems.

An initial sill intrusion is introduced at a depth $z = H$ (Fig. 3). The lithostatic pressure (P_L) is assumed to be known and hydrostatic ($\sigma_{xx} = \sigma_{yy} = \sigma_{zz}$). Therefore, only the unknown deviation from the lithostatic stress state, $\Delta\sigma_{ij}$, is calculated in the simulation. The actual stress is the sum of the two components:

$$\sigma_{ij} = \Delta\sigma_{ij} + P_L\delta_{ij} \qquad \text{Eq. 1}$$

where the indices $i, j = x, y, z$ and δ_{ij} is the identity tensor (1 if $i = j$ and 0 otherwise). Compressive stress here is reckoned positive; tensile stress is negative. This separation of the stress state into two components allows better representation of the conditions at the sill tip, which is critical for modelling the evolution of sills. In general, the magma pressure in the sill and the applied tectonic stress will enhance the stress at the sill tip, whereas the lithostatic pressure will not.

2.2. Failure Criteria

The sill intrusion process is analogous to the growth of a crack filled with a pressurised fluid (Bunger et al, 2008). Here it is assumed that the stress state near the sill (crack) tip cannot be resolved accurately, partly because the appropriate lower length scale cannot be resolved in a computationally tractable model, but also because the exact nature of the local crack tip conditions is not well understood. For example, heating due to the magma may lead to localised non-linearity (e.g. viscoplasticity; Souche et al., 2019), thermal expansion, and water vaporisation in wet rocks (e.g., Pollard et al., 1975; Schofield et al., 2010; Galland et al., 2019). The stress at the sill tip is expected to be considerably larger than the stress resolved in a discrete continuum model with a fixed mesh size. Here it is assumed that the actual stress is proportional to the stresses at the tip resolved in the model through a constant $\alpha > 1$, such that the locally enhanced stresses at the sill tip are given by:

$$\sigma_{ij}^{tip} = \alpha\Delta\sigma_{ij}^{tip} + P_L\delta_{ij} \qquad \text{Eq. 2}$$

Two failure criteria are adopted. For brittle tensile fracture, we assume that failure occurs when:

$$\sigma_3^{tip} = \sigma_T \qquad \text{Eq. 3}$$

where σ_3 is the minimum compressive stress (where principal stresses $\sigma_3 \leq \sigma_2 \leq \sigma_1$) and $\sigma_T < 0$ is the tensile failure strength of the material. Using Equation 1 gives the equivalent condition in the model as:

$$\Delta\sigma_3^{tip} = \frac{1}{\alpha}(\sigma_T - P_L) \quad . \qquad \text{Eq. 4}$$

To induce sill growth in the model, a fixed source overload pressure P_o is applied to the root of the initial intrusion at $z = 0$ (Fig. 3). In general, the overpressure is not known, as the value required to initiate sill intrusion depends on the depth at which this occurs, the precise physical conditions at the sill tip (for instance tip geometry, and temperature) and the fracture toughness of the rock. In this model, the choice of P_o can be made arbitrarily without affecting the final outcome; it is simply a reference stress against which the relative magnitude of the other stresses in the model are defined. When no tectonic stress is applied, the observed stress required to initiate tensile failure in the model will therefore be proportional to this overpressure, i.e. $\Delta\sigma_3^{tip} = -\beta P_o$, where β is a constant. The sill starts at a depth H so that at first failure Equation 4 gives a sill tip stress enhancement factor of $\alpha = \frac{(\rho g H - \sigma_T)}{\beta P_o}$, and the tensile failure condition becomes:

$$\Delta\sigma_3^{tip} = \sigma_f^{FE}(z) \qquad \text{Eq. 5}$$

where $\sigma_f^{FE}(z) = -\beta P_O \left(\frac{\rho g z - \sigma_T}{\rho g H - \sigma_T}\right)$, which reduces as the sill climbs towards the free surface (at $z = 0$). The FE superscript is used to indicate properties that are calibrated for the FE simulation. They are not to be confused with the actual physical parameter itself, although these are used to determine the parameter in the FE simulation relative to the chosen magma overpressure P_o.

For shear failure, we assume the Mohr-Coulomb relationship

$$\tau_f = \sigma_n tan\phi + C\ , \qquad \text{Eq. 6}$$

where the failure shear stress τ_f depends on the cohesive strength C, the angle of internal friction ϕ, and the normal stress σ_n acting on the plane. The optimal slip condition is:

$$\tau_{max} = P_{max} sin\phi + C cos\phi\ , \qquad \text{Eq. 7}$$

where the maximum shear stress $\tau_{\max}$ is

$$\tau_{max} = \frac{1}{2}\left(\sigma_1^{tip} - \sigma_3^{tip}\right) = \frac{\alpha}{2}\left(\Delta\sigma_1^{tip} - \Delta\sigma_3^{tip}\right)\ , \qquad \text{Eq. 8}$$

and the hydrostatic stress $P_{\max}$ is

$$P_{max} = \frac{1}{2}\left(\sigma_1^{tip} + \sigma_3^{tip}\right) = \frac{\alpha}{2}\left(\Delta\sigma_1^{tip} + \Delta\sigma_3^{tip}\right) + P_L\ . \qquad \text{Eq. 9}$$

Therefore the Mohr-Coulomb condition is written as:

$$\frac{1}{2}(1 - \sin\phi)\Delta\sigma_1^{tip} - \frac{1}{2}(1 + sin\phi)\Delta\sigma_3^{tip} = \frac{1}{\alpha}(P_L sin\phi + C cos\phi)\ . \qquad \text{Eq. 10}$$

As in the tensile failure case, this is also scaled relative to the overpressure. For an assumed friction angle of $\phi = 30^o$, this gives

$$\frac{1}{4}\left(\Delta\sigma_1^{tip} - 3\Delta\sigma_3^{tip}\right) = \tau_f^{FE}(z) \qquad \text{Eq. 11}$$

where $\tau_f^{FE}(z) = \beta P_o \left(\frac{\rho g z + \sqrt{3}C}{2(\rho g H - \sigma_T)}\right)$.

The critical failure stresses for determining the initial growth and onset of climbing for a sill are those determined at the starting depth H. Given that typically $\sigma_T \ll \rho g H$, the ratio of the shear failure stress to the tensile failure stress, ψ, can be expressed for a general friction angle as

$$\psi = \frac{\tau_f^{FE}(H)}{\sigma_f^{FE}(H)} \approx sin\phi + \left(\frac{C}{\rho g H}\right) cos\phi. \quad \text{Eq. 12}$$

This factor determines whether the shear (small ψ) or tensile (large ψ) failure criteria is dominant.

2.3. The damage model

Rock fracture is simulated by a crack-band damage model (e.g., Bazant and Oh, 1983), whereby the damage parameter $0 \leq D \leq 1$ characterises the level of fracture at a point, with $D = 0$ representing fully intact rock and $D = 1$ representing completely failed rock. Damage only occurs near the sill tip where the stress is enhanced (by factor α). The tip region is taken to be the 7 x 7 square of mesh elements surrounding the current element where damage is occurring (Fig. 3). The damage parameter evolves in these elements according to:

$$\frac{\partial D}{\partial t} = k_D \quad \text{Eq. 13}$$

where the rate constant is $k_D = 100\ s^{-1}$ if either failure condition (Equation 5 or 11) is satisfied in the tip region, and zero otherwise. The value of D is capped so it cannot exceed one. The damage affects the linear elastic analysis through adaptation of the Young's modulus E (e.g., Heap et al., 2010) such that

$$E = E_r(1 - D)\ , \quad \text{Eq. 14}$$

where E_r is the modulus of the unfractured rock. This means that the fractured rock has no mechanical stiffness when the differential stress is in tension. The failure conditions, Equations 5 and 11, are determined using stresses calculated directly from the strains using the undamaged modulus, E_r. This is necessary as the reduced modulus of Equation 14 causes the stresses in a damaged region to decrease causing failure to halt, whereas the strains increase (as the crack opens) allowing failure to continue.

2.4. Magma pressure and fluid flow

We assume that the magma flows down a pressure gradient following Darcy's law such that the fluid flux is given by

$$j_i = -k_{ij}\left(\frac{\partial P}{\partial x_j} - \rho a_j\right) \quad \text{Eq. 15}$$

where k_{ij} is the permeability tensor, and the only non-zero contribution from the acceleration is that due to gravity such that $a_z = -g$. We define the total pressure as $P_m = P_L + \Delta P$. Mass conservation requires an incompressible fluid satisfies:

$$\frac{\partial \epsilon_V}{\partial t} = -\frac{\partial j_i}{\partial x_i} = \frac{\partial}{\partial x_i}\left(k_{ij}\frac{\partial \Delta P}{\partial x_j}\right) \quad \text{Eq. 16}$$

where ϵ_V is the volumetric strain in the magma channel. This stiff system is difficult to implement numerically and it is more practical to consider the magma as a slightly compressible fluid such that

$$\frac{\partial \Delta P}{\partial t} = K_f\left[\frac{\partial}{\partial x_i}\left(k_{ij}\frac{\partial \Delta P}{\partial x_j}\right) - \frac{\partial \epsilon_V}{\partial t}\right], \quad \text{Eq. 17}$$

where K_f is the bulk modulus of the fluid. It is common to assume that the magnitude of the permeability tensor is given by $k_P = \frac{w^3}{12\mu}$, where w is the width of the magma channel and μ is the magma viscosity (Witherspoon et al., 1980; Chen et al., 2017). Tests with permeability anisotropy (normal and perpendicular to the channel) showed that the sill geometry is not sensitive to this parameter, and permeability is therefore taken to be isotropic, i.e. $k_{ij} = \eta k_P \delta_{ij}$, where the parameter η is zero until an element is fully damaged, at which point it is set to unity. The channel width is taken to be $w = w_0(1 + \epsilon_3)$ where ϵ_3 is the minimum shortening (maximum elongation) principal strain in the channel and w_0 is the initial width of the intrusion. The dependence of the permeability on η restricts the fluid flow to the damaged (intrusion) zone.

The magma overpressure $\eta\Delta P\delta_{ij}$ is added to the stress state of the simulation, where η ensures that the overpressure ΔP is only applied to the magmatic region. A positive (upward) body force of $f_z = \eta\Delta\rho g$ is added to the body, to model the buoyancy force of the magma, where $\Delta\rho = \rho_r - \rho_m$ is the difference between the density of the rock (ρ_r) and that of the magma (ρ_m), though this should have little contribution to the model relative to the magma overpressure (*cf.* Rubin, 1995).

2.5. Simulation parameters

The model has been implemented using the commercial FE software package COMSOL Multiphysics v5.3. Linear 4-noded square elements of side length $w_o = \frac{1}{50}H$ (Fig. 3) are employed for all three physical processes, where H is the initial depth of the intrusion. The simulations are axisymmetric and conducted within a large domain $8H$ deep by $16H$ radius to avoid boundary effects (Fig. 3). An initial horizontal rectangular intrusion of width w_o and radius $5w_o$ is introduced at the depth of H. The Young's modulus (E_r) of the rock is taken as 1 GPa, with a Poisson's ratio (ν) of 0.4. Magma viscosity (μ) is constant at 10^6 Pa·s and the bulk modulus of the magma (K_f) is 0.1 GPa. The rock tensile strength (σ_T) is –3 MPa, and the Mohr-Coulomb parameters are a shear cohesion (C) and an angle of internal friction (ϕ) of 30°. The rock density (ρ_r) is 2.5 g/cm^3 and the magma density (ρ_m) is 2.3 g/cm^3. This value for magma density would be reasonable for high silica-content magmas, but low for basaltic melts (Stolper and Walker, 1980; Bottinga et al., 1982); notably the 'magma' in our model has not traversed the column of denser crust and mantle lithosphere at depth, and a relatively low density is therefore justified here. A horizontal strain $\epsilon_r = \frac{(1-\nu)\sigma_r}{E_r}$ is applied to the outer radius of the simulation, where σ_r is the applied horizontal tectonic stress excess to the lithostatic pressure.

We take a reference magmatic overpressure (P_o) of 5 MPa, with the two failure conditions defined by Equations 5 and 11. The failure stress required to induce tensile failure at the tip of the initial intrusion in the FE model ($\sigma_f^{FE}(H) = -\beta P_o$) is –6 MPa with this overpressure, giving $\beta = 1.2$. At a depth of $H = 2km$, P_L is 50 MPa giving a stress enhancement factor at the crack tip of $\alpha = \frac{50+3}{6} \approx 9$. This implies that the actual stresses at the sill tip required to activate tensile fracture are roughly nine times higher than those resolved in the simulation. This is to be expected given the actual tip shape may be much sharper than we can simulate here, and shows how this approach mitigates the

approximation incurred by not modelling the sill tip in detail. The applied source pressure P_o is constant in our models, though it should be noted that neither the magma pressure, nor the magma flux should be expected to remain constant in nature (Rivalta, 2010; Schopa and Annen, 2013; Kavanagh et al., 2015); here, we generate variable pressure decay profiles, which are strongly coupled to the modelled sill growth.

The critical stress in the FE model required to instigate Mohr-Coulomb failure at the chosen overpressure in the absence of an applied tectonic stress is found to be 3.8 MPa, compared with –6 MPa required to induce tensile failure. The critical value of ψ, defined by Equation 15, at which both shear and tensile failure are equally likely in the absence of tectonic stress is therefore $\psi = \frac{3.8}{6} = 0.63$. The value of this parameter depends on the ratio of $\frac{C}{\rho g H}$. We therefore consider two cases which cover the expected range of this parameter (Haug et al, 2018): (1) with a lower shear strength of C= 8 MPa, and H = 2km, giving $\frac{C}{\rho g H} = 0.16$ and $\psi = 0.63$ (Fig. 4); and (2) with a higher shear strength of C= 20 MPa, and H = 1km, giving $\frac{C}{\rho g H} = 0.8$ and $\psi = 1.19$ (Fig. 5).

3. RESULTS

Figures 4 and 5 show simulation results for sills emplaced at 2 km and 1 km respectively; in both cases the key variable is σ_r. In both experiments, sills intruded under lithostatic conditions resulted in the initial growth of a flat sill until some critical radius r_c (1.81-1.25: Table 1, Figs. 4-7), after which the sill climbed at a consistent angle θ of ~23-24°. Increasing σ_r in both experiments resulted in an increase in r_c, to a maximum of $\sim 5H$, and a decrease in θ, to ~1° (Table 1, Figs. 4-7). In the lower shear strength case ($\frac{C}{\rho g H} = 0.16$ and $\psi = 0.63$), increasing σ_r above 4 MPa resulted in the onset of a decrease in r_c and an increase in θ (Figs. 4, 6A, and 7A,B). Increasing $\frac{C}{\rho g H}$ and ψ appears to delay the onset of this transition beyond the range of σ_r magnitudes tested here (Figs. 5, 6B, and 7C,D).

Figure 6 demonstrates a transition in the overall sill profile as a function of σ_r. For experiments with relatively low host cohesion (Fig. 6A), sills emplaced where $\sigma_r < 4MPa$ show a concave profile in which θ decreases as the length of climb a_c increases; the curve of the profile is a 4th-5th order polynomial. Where $\sigma_r \geq 4MPa$, sills show a convex profile, in which θ increases with increasing length a_c; the curve simplifies to a 3rd order polynomial. For experiments with a relatively higher cohesion host, and at shallower depth, the transition from convex to concave occurs later, with only the $\sigma_r = 5MPa$ sill showing a concave form.

Numerous numerical tests were conducted to explore the influence of other parameters, including the host rock Poisson's ratio ν, permeability anisotropy (with vertical permeability increased by up to a factor of 100), magma bulk modulus and density (contributing to buoyancy), and mesh size within the region of the sill ($w_o = \left\{\frac{1}{100}, \frac{1}{50}, \frac{1}{25}\right\} H$). None of these parameters affected the overall sill geometry, with the buoyancy term and the lithostatic pressure resulting in a minor (i.e., close to uncertainty within the simulations) increase in the sill angle.

4. DISCUSSION

4.1. Comparison with analogue models

Bunger et al., (2008) conducted analogue experiments for sill intrusion, monitoring the axisymmetric crack radius and height over time as pressurised fluid was pumped into the crack at a fixed rate. Two materials were selected for the analogue rock (Glass and PMMA) with glycerine or glucose solution for the analogue magma. The sill was initiated from a flaw of 6 mm radius machined at the end of the injection tube, with sample depths in the range of 12 to 30 mm, i.e. $\frac{r}{H}$ = 0.2 to 0.5 initially. The effect

of a horizontal stress, equivalent to σ_r, on sill profiles was investigated. They introduced a dimensionless parameter χ as a means to define scale-independent factors affecting sill profiles

$$\chi = \frac{\sigma_r \sqrt{H}}{K_c} \quad \text{Eq. 18}$$

where in the case of Bunger et al., (2008) K_c is specifically the mode I fracture toughness K_{Ic} of the host material.

To compare the simulation results with the analogue model of Bunger et al (2008) it is necessary to determine the effective fracture toughness of the rock in the FE model. This can be calculated from the critical energy release rate, G_c. This method avoids the need to consider the details of the stress field around the sill tip. The critical energy release is defined as $G_c = \frac{dU}{dA}$, where U is the total change in elastic energy associated with an increase in the crack area A. The energy release rate in the simulations was constant, indicated by the constant slope in the U versus A plot in Fig. 9B. This shows that the magma pressure distribution evolved to keep the stress intensity K at the crack tip constant, i.e. $K = K_C$. This indicates that the sill growth is controlled by the toughness of the rock rather than the viscosity of the magma. The assumption that intrusions grow under constant K_C is supported by the crack length versus thickness calculations of Scholz (2010) for dykes and veins (from Schultz et al., 2008, and references therein). The effective (mode I or II) fracture toughness K_C can be inferred from the standard elastic relationship (Zehnder, 2012)

$$G_c = \frac{K_C^2}{E_r} \quad \text{Eq. 19}$$

yielding $K_C^{FE} = 26\ MPa\ \sqrt{m}$,where the FE superscript has again been employed to demonstrate that this is a simulation parameter not a physical one. This is related to the chosen failure stress by $K_C^{FE} = A\sigma_f^{FE}\sqrt{H}$, where the initial depth of the sill, H, is the characteristic length scale for the problem. For our chosen FE mesh the constant is A = 0.097. Thus, given $\sigma_f^{FE}(H) = -\beta P_o$, we can write the effective χ value determined from the FE model as

$$\chi^{FE} = B\frac{\sigma_r}{P_0} \quad \text{Eq. 20}$$

where $B = \frac{1}{A\beta}$= 8.6 is a dimensionless constant. This shows that the ratio of the applied tectonic stress to the magma overpressure determines the large-scale evolution of the sill. The constant B relates these FE simulations to the χ parameter of Bunger et al., (2008).

To generate results comparable with the analogue model of Bunger et al., (2008), the effects of lithostatic pressure and buoyancy are removed from the simulation, and failure is limited to mode I tensile fracture. The results are shown for PMMA and glass in Figure 8. It can be seen that the slopes of the sills are in very good agreement between the two models, although the difference in horizontal section length prior to this is considerable. There are a number of potential explanations for this difference: (1) the horizontal section in the analogue results is typically of the order of the initial flaw size ($0.2 < \frac{r}{H} < 0.5$) suggesting that there is little to no horizontal growth in their models; (2) the analogue cracks initiate from a machined notch which may not induce an initial horizontal crack; (3) the analogue cracks are not completely axisymmetric; (4) the fracture extends ahead of the fluid in the analogue case, possibly due to the action of capillary forces which are not significant in a full scale

FE model; and (5) the FE model requires a finite perturbation in the stress to destabilise horizontal sill growth.

The FE model of Equation 20 provides scaling behaviour for a blunt sill and predicts that the value of χ^{FE}=8.6 corresponds most closely with the Tulipan Sill (see Fig 5A) for which it is expected that the tectonic stress has the same value as the magma source overpressure ($\sigma_r = P_o$). The overpressure is not known accurately, but values of 0.5 to 6 MPa have been estimated elsewhere (Gudmundsson, 2012) with an average of 3 MPa and a maximum of 9 MPa. The higher end of this scale ($\geq$ 3 MPa) would appear to be a reasonable differential relative to a lithostatic pressure of 50 MPa at a depth of 2km, as one would expect it to be larger than natural variations in the hydrostatic stress state (Suppe, 1985). Using the expression of Bunger et al., (2008) from Equation 18, with a typical fracture toughness for sandstones at about 2 km depth of roughly 3 $MPa\sqrt{m}$ (Stoeckhert et al, 2016) predicts an applied tectonic stress of around 0.6 MPa for a value of $\chi = 8.6$. This is at the lower end of the expected range given above, and is a very small stress in comparison to the additionally imposed lithostatic pressure of 50 MPa. This analysis is based on a crack tip that is sharp, whereas in reality the tip of the sill would not be as sharp as a crack, leading to the higher value predicted by Equation 20 for the FE model.

4.2. Magma pressure distribution along the sill

The magma overpressure distribution (ΔP) within the intrusion for zero tectonic stress just before the sill leaves the horizontal plane is shown in Figure 9A. The source pressure at the root of the sill is fixed at $P_o = 5MPa$. The pressure drop along the sill causes magma to flow towards the tip. It can be seen that a small negative pressure has developed at the tip of the intrusion by this stage (Fig. 9A). This indicates that the sill crack grows at the tip faster than magma can readily accommodate the increase in volume, causing the magma to be sucked in to the tip region (*cf.* Rubin, 1995). The negative pressure will act to close the crack tip, but it is held open by the much more significant action of the positive pressure in the sill behind it. Alternatively, this could be considered a condition for separation of the fracture front and the magma front, i.e. the crack grows faster than the sill producing a tip cavity, which is not possible in this model but may occur in scaled analogue models and nature (e.g., Rubin, 1993; Liss et al., 2002; Kavanagh et al., 2006; Bunger et al., 2008).

We use the stress intensity factor for a penny-shaped crack in an infinite solid subjected to a varying internal pressure distribution $K_I = \frac{4}{\sqrt{\pi a}}\int_0^a \frac{P(r)}{\sqrt{a^2-r^2}} r dr$ (Sneddon, 1946) to generate another estimate for the fracture toughness of the rock in the FE simulation, where a is the current crack length. This yields a value of $K_C^{FE} = 25\ MPa\sqrt{m}$, in excellent agreement with the previous estimate, given that the analytical solution is for a crack in an infinite medium.

4.3. Energy release rates for different sill geometries

The intrusion simulations have shown that the model is quite insensitive to the material input parameters, with the sill incline θ demonstrating a strong preference for a particular orientation at a given tectonic stress. This suggests the elastic driving force due to the presence of the free surface and the tectonic stress are the primary controls on saucer-type sill shape. Here we explore the energy release rate of pressurised intrusion-like cracks as a function of their geometry and the pressure distribution within them. The axisymmetric sill geometry for a sill at depth H is described in terms of three parameters, illustrated in Figure 1D: the radius of the flat section of the sill, r_c, the length of the inclined section of the sill, a_c, and the climb angle of this section, θ. The normalised energy release rate is determined for different geometries and loading conditions for host rock with a Poisson ratio $\nu = 0.3$. A sill is expected to propagate in the direction which maximises the energy release rate.

4.3.1 Effect of internal pressure

The modelled sill is subject to an internal pressure distribution (e.g., Fig. 9A). Three different pressure distributions are investigated, each with smooth gradients; we do not consider abrupt pressure changes along the length of the sill, which would reflect significant viscosity variation within the conduit, which has been shown to have a marked effect on intrusion growth and geometry (Pollard and Johnson, 1973). We use the parameter $0 \leq s \leq 1$ to denote the location along the sill, with $s = 0$ at the root (at $r = 0$), increasing linearly over the total sill length of $r_c + a_c$, to $s = 1$ at the tip. The pressure distributions are: (1) constant pressure, $p(s) = P_0$; (2) linearly decaying pressure, $p(s) = 3P_0(1 - s)$; and (3) quadratic pressure decay, $p(s) = 6P_0(1 - s)^2$. The pre-factors have been chosen to keep the total force roughly similar between cases. These are expected to cover the extreme range of expected pressure distributions, with the quadratic pressure distribution being closest to that observed in this toughness-controlled model (see Figure 9A), and a constant pressure being closest to that postulated for a viscous-controlled model.

A sill is expected to grow at an inclined angle θ once the energy release rate is no longer maximum along the horizontal ($\theta = 0^o$). Figure 10A shows the normalised energy release rate, $\bar{G}_P = \frac{E_r}{P_o^2 H} G$, as a function of θ for $r_c = 1.5H$, a length at which the modelled sills are seen to initiate an incline. The energy release rate peaks at about 25-30° suggesting this is the angle at which the sill would climb if there were no other forces acting on it (e.g., buoyancy forces). This is also typically the angle found in the sill simulations in the case of zero applied tectonic stress (Figs. 6 and 7). The angle of inclination is largely insensitive to the pressure distribution, which explains the insensitivity of the simulation to the various parameters that might affect this, such as buoyancy forces, magma bulk modulus, and the magma permeability tensor.

Figure 10B shows the change in the normalised energy release rate, $\bar{G}_P$, when a flat sill begins to climb at 25° as a function of its flat section length; a positive energy change indicates that the switch is energetically favourable. It can be seen that the energetics for a switch are favourable for $r_C = 0.8H$ for the quadratic pressure distribution, rising to $r_C = 1.15H$ for the constant pressure distribution. In the FE model a sill length of $r_C = 1.5H$ is typically seen for zero tectonic stress (Fig. 6). This suggests that there is a finite energy barrier to be overcome to switch to inclined growth in the FE model, probably due to the sill having a blunt tip. In practice, there will also be localised stabilisation of horizontal natural sills due to host rock mechanical layering (e.g., Mudge, 1968; Johnson and Pollard, 1973; Burchardt, 2008).

In summary, the energy release rate calculations show that, in a linear elastic body, an axisymmetric sill will grow horizontally until its length exceeds 0.8-1.15 times its depth, which is dependent on the magma pressure distribution within the sill. In the absence of a tectonic stress, the sill will then climb at roughly 25-30° to the horizontal (Figs. 6, 7, and 10).

4.3.2 Effect of tectonic stress

A constant horizontal stress σ_r was applied to the remote vertical boundary, and the internal pressure on the crack removed. The applied stress will lead to a stress concentration at the crack tip, which if compressive will hinder the growth of the crack, and if tensile will assist its growth. The net differential stress (above lithostatic) is assumed to remain tensile, i.e. the pressure in the sill always acts to open the crack. Figure 10C shows the effect of the applied stress on the normalised energy release rate, $\bar{G}_r = \frac{E_r}{\sigma_r^2 H} G$, for a crack of length $r_C = 1.5H$ for different inclination angles θ=15°, 30°, 45° and 60° as a function of the inclined sill length a_c. The lines are almost linear such that Equation 18 suggests that the normalised stress intensity at the sill tip due to the tectonic stress is

$$\frac{K_r}{\sigma_r\sqrt{H}} = F\left(\theta, \frac{r_c}{H}\right)\sqrt{\frac{h}{H}} \qquad \text{Eq. 21}$$

where $h = a_c sin\theta$ is the height of the sill tip above its starting depth. This means that the applied stress has little effect on a horizontal sill, but that a compressive stress can stabilise horizontal sill growth by reducing the stress intensity at the sill tip as it starts to rise. This equation implies that the applied stress has greater effect as the sill grows towards the surface. This analysis does not identify how the mix of tensile and shear loading changes at the tip, with the contribution from the shear component expected to increase as the angle of incline gets larger.

Figure 10D shows the dimensionless pre-factor $F\left(\theta, \frac{r_c}{H}\right)$ for two different sill base lengths. This shows the expected result that a tensile differential tectonic stress ($\sigma_r < 0$) will act to drive an intrusion to climb at or near 90°, as this assists the stress intensity at the sill tip most at this angle. In compression ($\sigma_r > 0$), the reverse is the case, with the applied stress decreasing the stress intensity at the sill tip most effectively at 90°, hence driving the crack towards 0° as this reduces the stress intensity the least, allowing sills to continue to grow at these low angles.

These findings are summarised in the schematic illustration of Figure 11, which demonstrates that the differential stress (beyond lithostatic) at the tip of an inclined sill comes from two main contributions:

(1) The internal magma pressure ΔP generates the majority of the stress that fractures the host rock, and drives the sill forward. The stress intensity at the sill tip is proportional to the magma overpressure times the root length, in which the characteristic length is the starting depth. It has been shown that in a lithostatic stress state, the asymmetric stress field at the tip drives the sill to climb at an incline of about 25^o to the horizontal (Fig. 11A). This is the typical sill angle observed in models for sills conducted in the absence of a tectonic stress (e.g., Galland et al., 2009).

(2) The imposition of a horizontal tectonic stress creates an additional stress field that is superimposed on the tip (Fig. 11B), with the stress intensity proportional to the applied stress times the root of the height above the initial sill. If the differential tectonic stress is compressive ($\sigma_r > 0$) then it has been shown that the stresses at the sill tip are reduced, with the maximum reduction applying to vertical intrusions and the minimum reduction for horizontal intrusions. A compressive applied tectonic stress therefore drives the sill to a shallower angle of incline, and a tensile tectonic stress drives the intrusion towards higher angles of incline.

5. CONCLUSIONS

Our numerical simulations of saucer-shaped sills show that tectonic stress has a first order control on intrusion geometry, with compressive stresses subduing the effect of asymmetric tip stress generated through interaction with the free surface. Our results are in good agreement with analogue models of fluid-filled cracks presented by Bunger et al., (2008), indicating this is a scalable phenomenon. Increasing horizontal compressive stress results initially in an increase in the saucer base length, and a decrease in the angle of incline beyond this base; further increases in the horizontal stress result in a switch to extensional shear failure, a decrease in base length and an increase in the sill incline. In our simulations, sills are most closely matched to natural examples, when the magnitude of tectonic stress above lithostatic is equal to the magma overpressure within the sill; applied tectonic stresses above or below this value result in steeper sills. Sill incline relates to the angle of maximum energy release rate, which is also affected by the magma pressure distribution within the sill.

REFERENCES

Amelung, F., Jónsson, S., Zebker, H. and Segall, P., 2000. Widespread uplift and 'trapdoor'faulting on Galapagos volcanoes observed with radar interferometry. Nature, 407(6807), p.993.

Bažant, Z.P. and Oh, B.H., 1983. Crack band theory for fracture of concrete. Matériaux et construction, 16(3), pp.155-177.

Bottinga, Y., Weill, D. and Richet, P., 1982. Density calculations for silicate liquids. I. Revised method for aluminosilicate compositions. Geochimica et Cosmochimica Acta, 46(6), pp.909-919.

Bunger, A.P., Jeffrey, R.G. and Detournay, E., 2008. Evolution and morphology of saucer-shaped sills in analogue experiments. Geological Society, London, Special Publications, 302(1), pp.109-120.

Burchardt, S., 2008. New insights into the mechanics of sill emplacement provided by field observations of the Njardvik Sill, Northeast Iceland. Journal of Volcanology and Geothermal Research, 173(3-4), pp.280-288.

Chen, T., Cheng, S., Fang, Q. and Zhou, C., 2017. Numerical modeling of shallow magma intrusions with finite element method. Journal of Volcanology and Geothermal Research, 333, pp.53-65.

Galland, O. and Scheibert, J., 2013. Analytical model of surface uplift above axisymmetric flat-lying magma intrusions: Implications for sill emplacement and geodesy. Journal of Volcanology and Geothermal Research, 253, pp.114-130.

Galland, O., Planke, S., Neumann, E.R. and Malthe-Sørenssen, A., 2009. Experimental modelling of shallow magma emplacement: Application to saucer-shaped intrusions. Earth and Planetary Science Letters, 277(3-4), pp.373-383.

Galland, O., Spacapan, J.B., Rabbel, O., Mair, K., Soto, F.G., Eiken, T., Schiuma, M. and Leanza, H.A., 2019. Structure, emplacement mechanism and magma-flow significance of igneous fingers–Implications for sill emplacement in sedimentary basins. Journal of Structural Geology, 124, pp.120-135.

Gudmundsson, A., 2012. Magma chambers: Formation, local stresses, excess pressures, and compartments. Journal of Volcanology and Geothermal Research, 237, pp.19-41.

Hansen, J., 2015. A numerical approach to sill emplacement in isotropic media: Do saucer-shaped sills represent 'natural'intrusive tendencies in the shallow crust?. Tectonophysics, 664, pp.125-138.

Hansen, J. 2011. Petrogenetic Evolution, Geometries and Intrusive Styles of the Early Cenozoic Saucer-Shaped Sills of the Faroe Islands. Doctoral thesis, Durham University.

Haug, Ø.T., Galland, O., Souloumiac, P., Souche, A., Guldstrand, F. and Schmiedel, T., 2017. Inelastic damage as a mechanical precursor for the emplacement of saucer-shaped intrusions. Geology, 45(12), pp.1099-1102

Haug, Ø.T., Galland, O., Souloumiac, P., Souche, A., Guldstrand, F., Schmiedel, T. and Maillot, B., 2018. Shear Versus Tensile Failure Mechanisms Induced by Sill Intrusions: Implications for Emplacement of Conical and Saucer-Shaped Intrusions. Journal of Geophysical Research: Solid Earth, 123(5), pp.3430-3449.

Heap, M.J., Faulkner, D.R., Meredith, P.G. and Vinciguerra, S., 2010. Elastic moduli evolution and accompanying stress changes with increasing crack damage: implications for stress changes around fault zones and volcanoes during deformation. Geophysical Journal International, 183(1), pp.225-236.

Jackson, M.D., Blundy, J. and Sparks, R.S.J., 2018. Chemical differentiation, cold storage and remobilization of magma in the Earth's crust. Nature, 564(7736), p.405.

Johnson, A.M. and Pollard, D.D., 1973. Mechanics of growth of some laccolithic intrusions in the Henry mountains, Utah, I: field observations, Gilbert's model, physical properties and flow of the magma. Tectonophysics, 18(3-4), pp.261-309.

Kavanagh, J.L., Menand, T. and Sparks, R.S.J., 2006. An experimental investigation of sill formation and propagation in layered elastic media. Earth and Planetary Science Letters, 245(3-4), pp.799-813.

Kavanagh, J.L., Boutelier, D. and Cruden, A.R., 2015. The mechanics of sill inception, propagation and growth: Experimental evidence for rapid reduction in magmatic overpressure. Earth and Planetary Science Letters, 421, pp.117-128.

Leat, P.T., 2008. On the long-distance transport of Ferrar magmas. Geological Society, London, Special Publications, 302(1), pp.45-61.

Liss, D., Hutton, D.H. and Owens, W.H., 2002. Ropy flow structures: A neglected indicator of magma-flow direction in sills and dikes. Geology, 30(8), pp.715-718.

Maclennan, J., 2019. Mafic tiers and transient mushes: evidence from Iceland. Philosophical Transactions of the Royal Society A, 377(2139), p.20180021.

Malthe-Sørenssen, A., Planke, S., Svensen, H., Jamtveit, B., Breitkreuz, C. and Petford, N., 2004. Formation of saucer-shaped sills. Physical geology of high-level magmatic systems. Geological Society, London, Special Publications, 234, pp.215-227.

Moy, D. 2010. The architecture, growth and tectono-stratigraphic significance of rift-oblique lineaments on the NE Atlantic Margin. Doctoral thesis, Durham University.

Moy, D.J. and Imber, J., 2009. A critical analysis of the structure and tectonic significance of rift-oblique lineaments ('transfer zones') in the Mesozoic–Cenozoic succession of the Faroe–Shetland Basin, NE Atlantic margin. Journal of the Geological Society, 166(5), pp.831-844.

Mudge, M.R., 1968. Depth control of some concordant intrusions. Geological Society of America Bulletin, 79(3), pp.315-332.

Muirhead, J.D., Airoldi, G., White, J.D. and Rowland, J.V., 2014. Cracking the lid: Sill-fed dikes are the likely feeders of flood basalt eruptions. Earth and Planetary Science Letters, 406, pp.187-197.

Planke, S., Rasmussen, T., Rey, S.S. and Myklebust, R., 2005, January. Seismic characteristics and distribution of volcanic intrusions and hydrothermal vent complexes in the Vøring and Møre basins. In Geological Society, London, Petroleum Geology Conference series (Vol. 6, No. 1, pp. 833-844). Geological Society of London.

Pollard, D.D. and Johnson, A.M., 1973. Mechanics of growth of some laccolithic intrusions in the Henry Mountains, Utah, II: bending and failure of overburden layers and sill formation. Tectonophysics, 18(3-4), pp.311-354.

Pollard, D.D., Muller, O.H. and Dockstader, D.R., 1975. The form and growth of fingered sheet intrusions. Geological Society of America Bulletin, 86(3), pp.351-363.

Polteau, S., Mazzini, A., Galland, O., Planke, S. and Malthe-Sørenssen, A., 2008. Saucer-shaped intrusions: Occurrences, emplacement and implications. Earth and Planetary Science Letters, 266(1-2), pp.195-204.

Rivalta, E., 2010. Evidence that coupling to magma chambers controls the volume history and velocity of laterally propagating intrusions. Journal of Geophysical Research: Solid Earth, 115(B7).

Rubin, A.M., 1993. Tensile fracture of rock at high confining pressure: implications for dike propagation. Journal of Geophysical Research: Solid Earth, 98(B9), pp.15919-15935.

Rubin, A.M., 1995. Propagation of magma-filled cracks. Annual Review of Earth and Planetary Sciences, 23(1), pp.287-336.

Schofield, N., Stevenson, C. and Reston, T., 2010. Magma fingers and host rock fluidization in the emplacement of sills. Geology, 38(1), pp.63-66.

Scholz, C.H., 2010. A note on the scaling relations for opening mode fractures in rock. Journal of Structural Geology, 32(10), pp.1485-1487.

Schultz, R.A., Soliva, R., Fossen, H., Okubo, C.H. and Reeves, D.M., 2008. Dependence of displacement–length scaling relations for fractures and deformation bands on the volumetric changes across them. Journal of Structural Geology, 30(11), pp.1405-1411.

Schöpa, A. and Annen, C., 2013. The effects of magma flux variations on the formation and lifetime of large silicic magma chambers. Journal of Geophysical Research: Solid Earth, 118(3), pp.926-942.

Sigmundsson, F., Hreinsdóttir, S., Hooper, A., Árnadóttir, T., Pedersen, R., Roberts, M.J., Óskarsson, N., Auriac, A., Decriem, J., Einarsson, P. and Geirsson, H., 2010. Intrusion triggering of the 2010 Eyjafjallajökull explosive eruption. Nature, 468(7322), p.426.

Sneddon, I.N., 1946. The distribution of stress in the neighbourhood of a crack in an elastic solid. Proceedings of the Royal Society of London. Series A. Mathematical and Physical Sciences, 187(1009), pp.229-260.

Souche, A., Galland, O., Haug, Ø.T. and Dabrowski, M., 2019. Impact of host rock heterogeneity on failure around pressurized conduits: Implications for finger-shaped magmatic intrusions. Tectonophysics, 765, pp.52-63.

Stoeckhert, F., Molenda, M., Brenne, S. and Alber, M., 2015. Fracture propagation in sandstone and slate–Laboratory experiments, acoustic emissions and fracture mechanics. Journal of Rock Mechanics and Geotechnical Engineering, 7(3), pp.237-249.

Stolper, E. and Walker, D., 1980. Melt density and the average composition of basalt. Contributions to Mineralogy and Petrology, 74(1), pp.7-12.

Suppe, J., 1985. Principles of structural geology. Prentice Hall.

Stephens, T.L., Walker, R.J., Healy, D., Bubeck, A., England, R.W. and McCaffrey, K.J., 2017. Igneous sills record far-field and near-field stress interactions during volcano construction: Isle of Mull, Scotland. Earth and Planetary Science Letters, 478, pp.159-174.

Stephens, T.L., Walker, R.J., Healy, D., Bubeck, A. and England, R.W., 2018. Mechanical models to estimate the paleostress state from igneous intrusions. Solid earth.

Walker, R.J., 2016. Controls on transgressive sill growth. Geology, 44(2), pp.99-102

Walker, R.J., Healy, D., Kawanzaruwa, T.M., Wright, K.A., England, R.W., McCaffrey, K.J.W., Bubeck, A.A., Stephens, T.L., Farrell, N.J.C. and Blenkinsop, T.G., 2017. Igneous sills as a record of horizontal shortening: The San Rafael subvolcanic field, Utah. GSA Bulletin, 129(9-10), pp.1052-1070.

Witherspoon, P.A., Wang, J.S., Iwai, K. and Gale, J.E., 1980. Validity of cubic law for fluid flow in a deformable rock fracture. Water resources research, 16(6), pp.1016-1024.

Zehnder, A.T., 2007. Lecture notes on fracture mechanics. Cornell University, 20

Figures

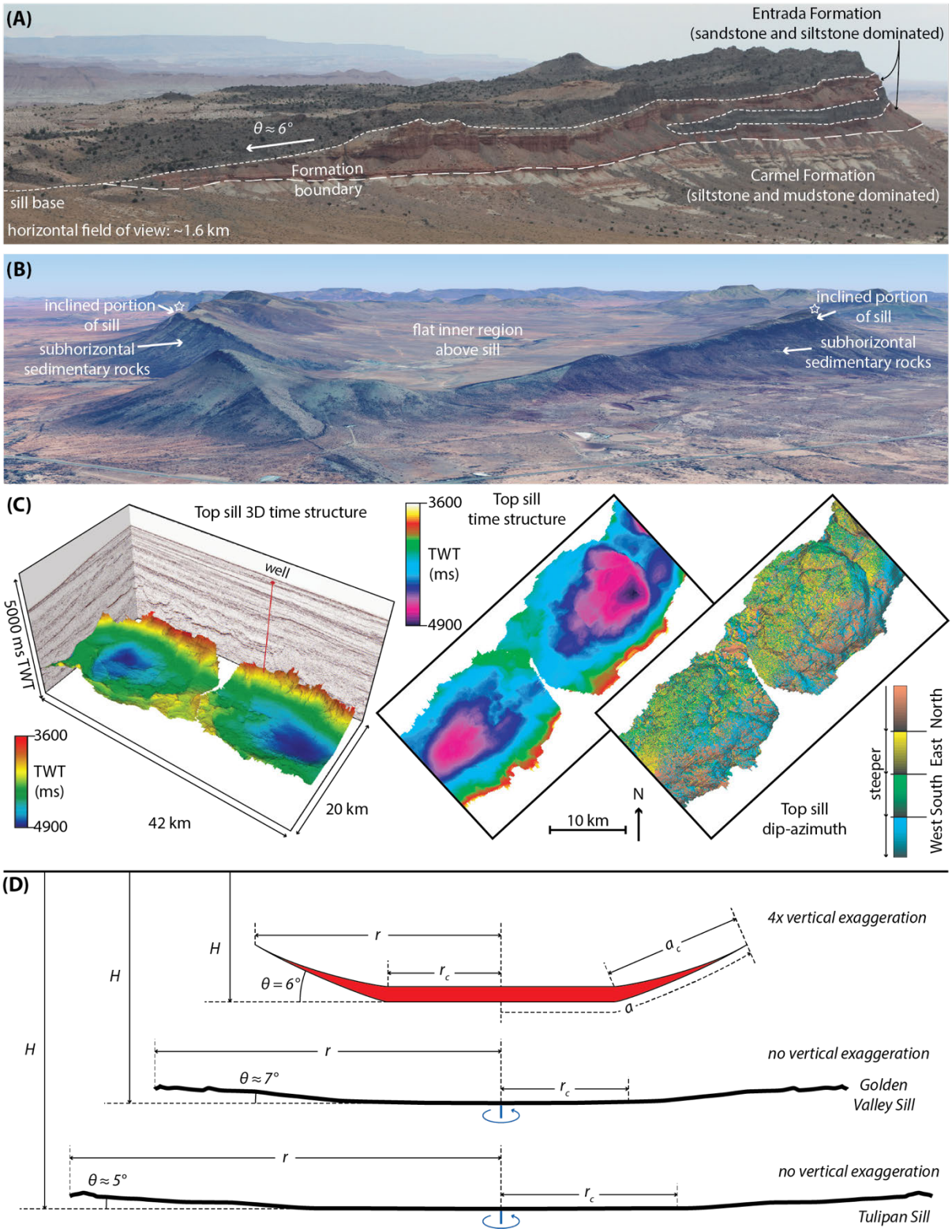

Figure 1. Natural sill geometries. (**A**) Flat to gently-transgressive sills in the San Rafael Sub-Volcanic Field, Utah USA, cuts the formation boundary separating Carmel Formation mudstones and siltstones below, and Entrada Formation sandstones and siltstones above. (**B**) The Golden Valley saucer-shaped sill, South Africa, emplaced at ~2.4 km depth into Permian-Triassic age, sub-horizontal sedimentary rocks (Polteau et al., 2008). The distance between the white stars is ~7 km (GoogleEarth image; map data: © CNES/Airbus, © Landsat/Copernicus, © 2019 Digital Globe). (**C**) Saucer-shaped sills in the

Faroe-Shetland Basin, imaged in seismic datasets (after Moy and Imber, 2009; Moy, 2010). Left-hand image is a 3D two-way-time (TWT) map of the sill top reflector. Middle and right-hand images are 2D top-sill time structure and dip-azimuth maps respectively. (**D**) Conceptual 2D cross-section illustrating the dimensions and main components of a saucer-shaped sill. Profiles for the Golden Valley Sill and Tulipan Sill (after Galland et al., 2009) are reflected about the centre point for illustration purposes.

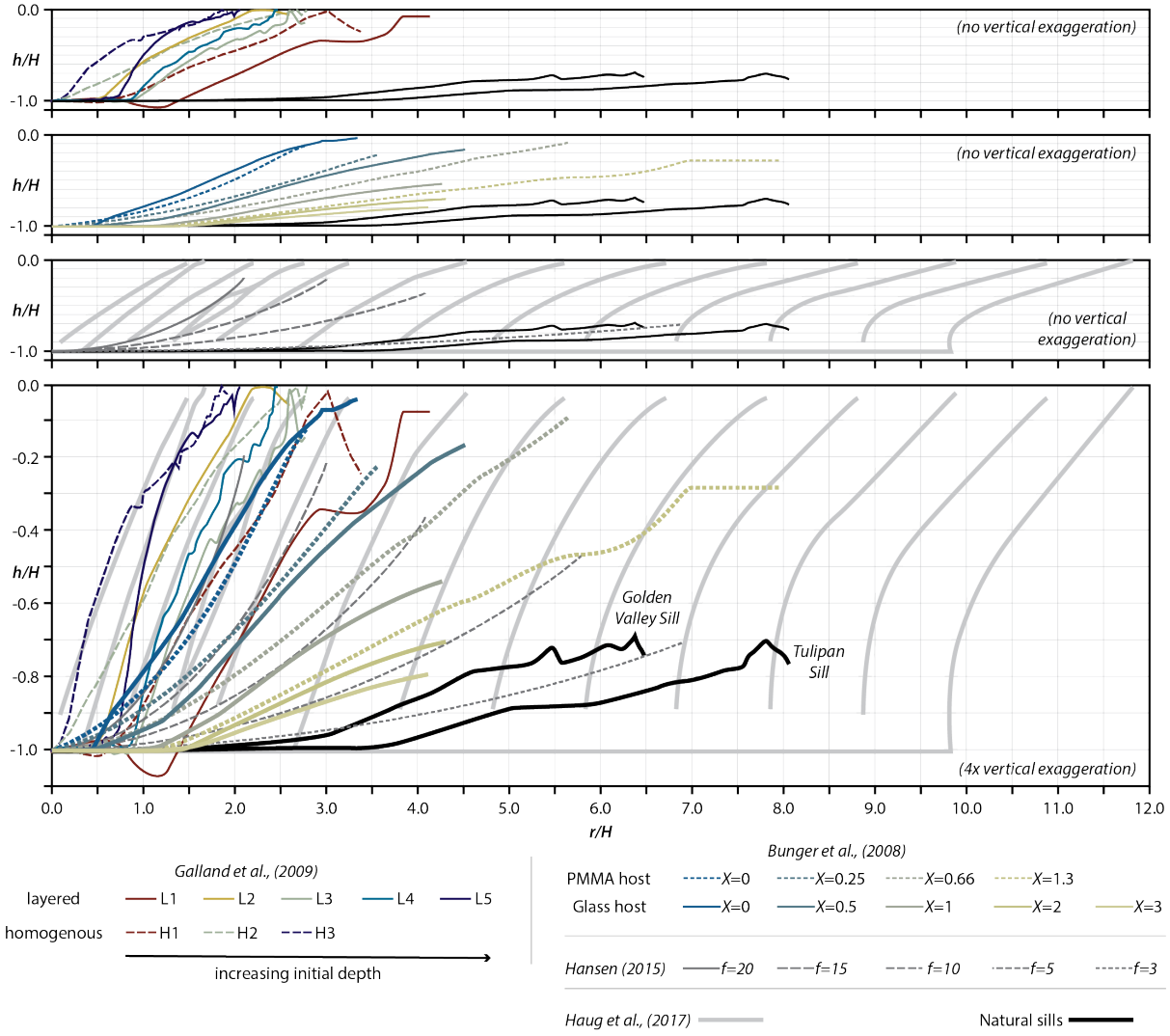

Figure 2. Comparison of natural and modelled sill profiles. Axes of sill radius r and depth h are normalized to the depth of emplacement H of the initial sill, for comparison (see Bunger et al., 2008). Galland et al., 2009 used silica powder and vegetable oil as the host rock and magma analogues respectively. Bunger et al., (2008) used glass or polymethyl methacrylate (PMMA) as the rock analogue, and water as the magma analogue. Their tests involved a deviatoric stress, applied as a horizontal radial stress during sill growth, and introduced a dimensionless parameter χ to consider scaling, where $\chi = \sigma_r\sqrt{H}/K_c$. The fracture toughness K_c is 1.3 and 0.6 MPa m$^{1/2}$ for their PMMA and glass respectively. Haug et al., (2017) simulated static cracks in a homogenous Mohr-Coulomb material; individual plots show the damage associated with cracks of different starting lengths, each with a starting depth $H = 2km$ and sill thickness $T = 50m$. Hansen (2015) calculated inflation sequences (IS) for elastic displacements above (D_U) and below (D_L) the intrusion centre line for isotropic host rocks as a function of the depth-dependent increase in Young's Modulus E, where $IS = f\frac{D_U+D_L}{2}$; f is simply a multiplication factor used to vary IS. Results are shown for his models as a function of f, with a magma overpressure $P_o = 10MPa$.

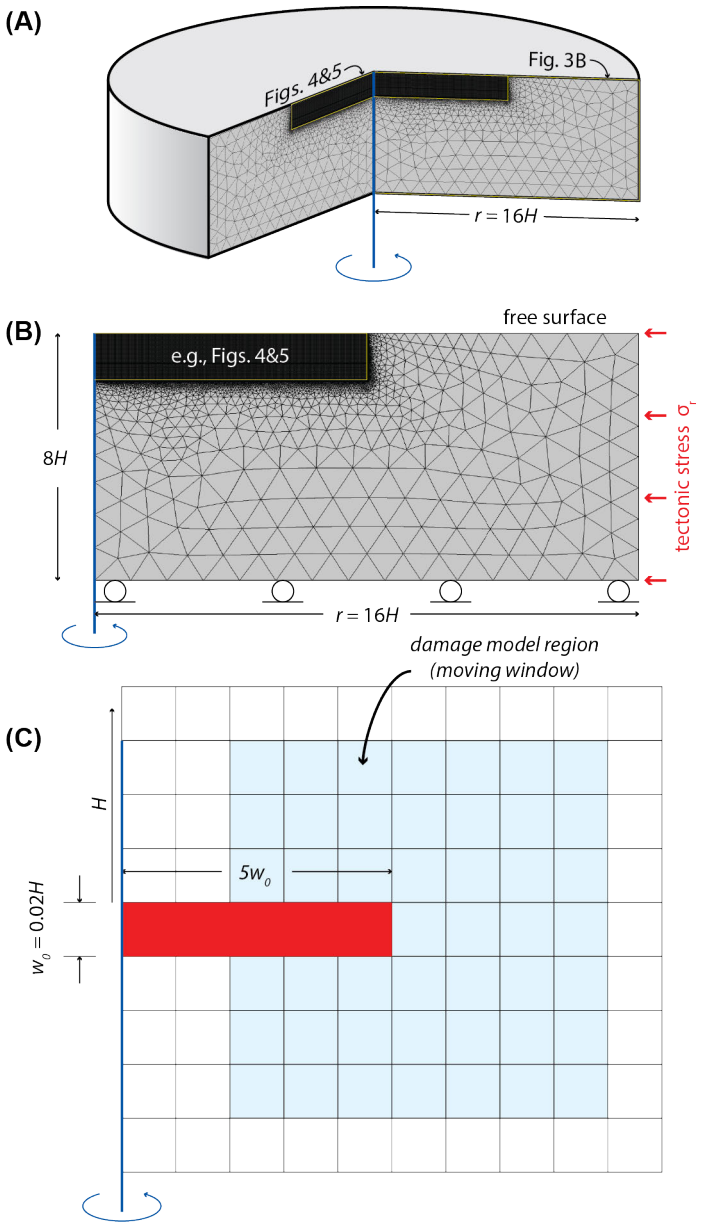

Figure 3. The model set-up. (**A**) Sills are modelled in an axisymmetric space with radius $16H$ and depth $8H$. The top surface is unbounded. (**B**) Cross section of the model radius showing structured squared-noded mesh in the region of the sill, and unstructured mesh to move the model boundaries far from the sill. (**C**) Example of the square-noded mesh with initial sill (red-shaded region) at depth H with starting thickness $w_o = \frac{1}{50}H$, and starting length $5w_o$. Blue-shaded region is the area of modelled damage associated with the sill tip.

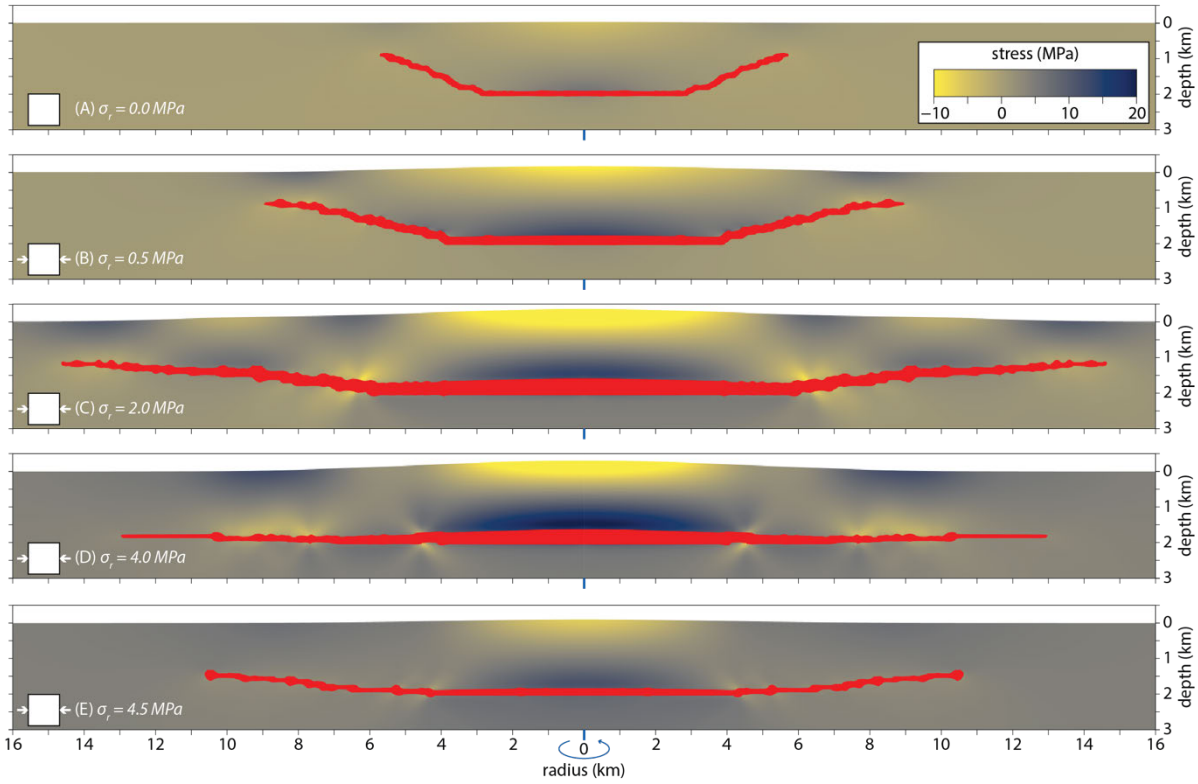

Figure 4. Numerical simulation results for sills seeded at 2 km $\psi = 0.63$ and $\frac{C}{\rho g H} = 0.16$, where σ_r is (**A**) 0.0 MPa, (**B**) 0.5 MPa, (**C**) 2.0 MPa, (**D**) 4.0 MPa, and (**E**) 4.5 MPa. The sill is shown in red; the colour key for stress is consistent for all of the simulations displayed. Note that the stress is the perturbation only.

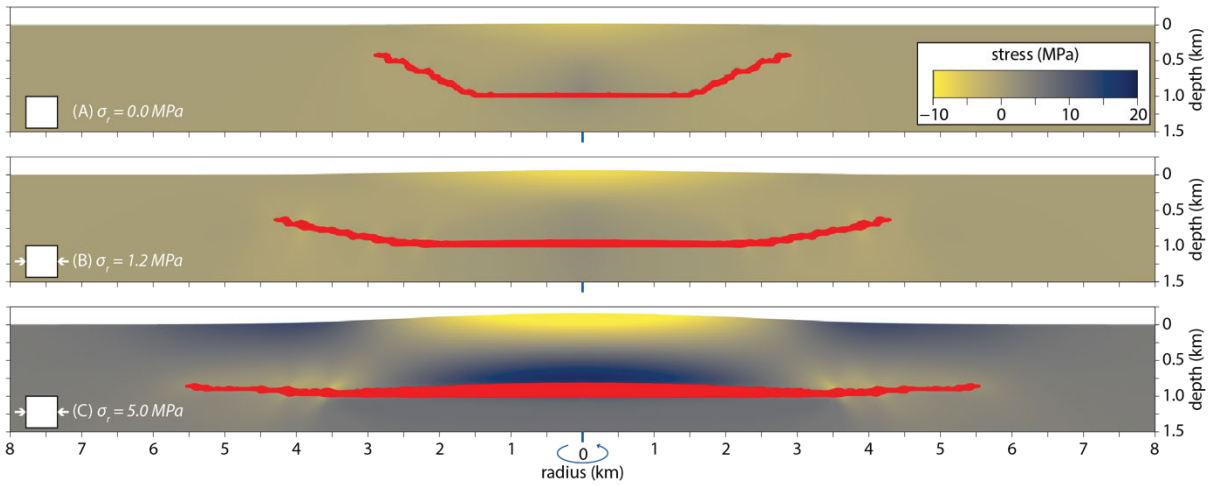

Figure 5. Numerical simulation results for sills seeded at 1 km $\psi = 1.19$ and $\frac{C}{\rho g H} = 0.8$, where σ_r is (**A**) 0.0 MPa, (**B**) 1.2 MPa, and (**C**) 5.0 MPa. The sill is shown in red; the colour key for stress is consistent for all of the simulations displayed. Note that the stress is the perturbation only.

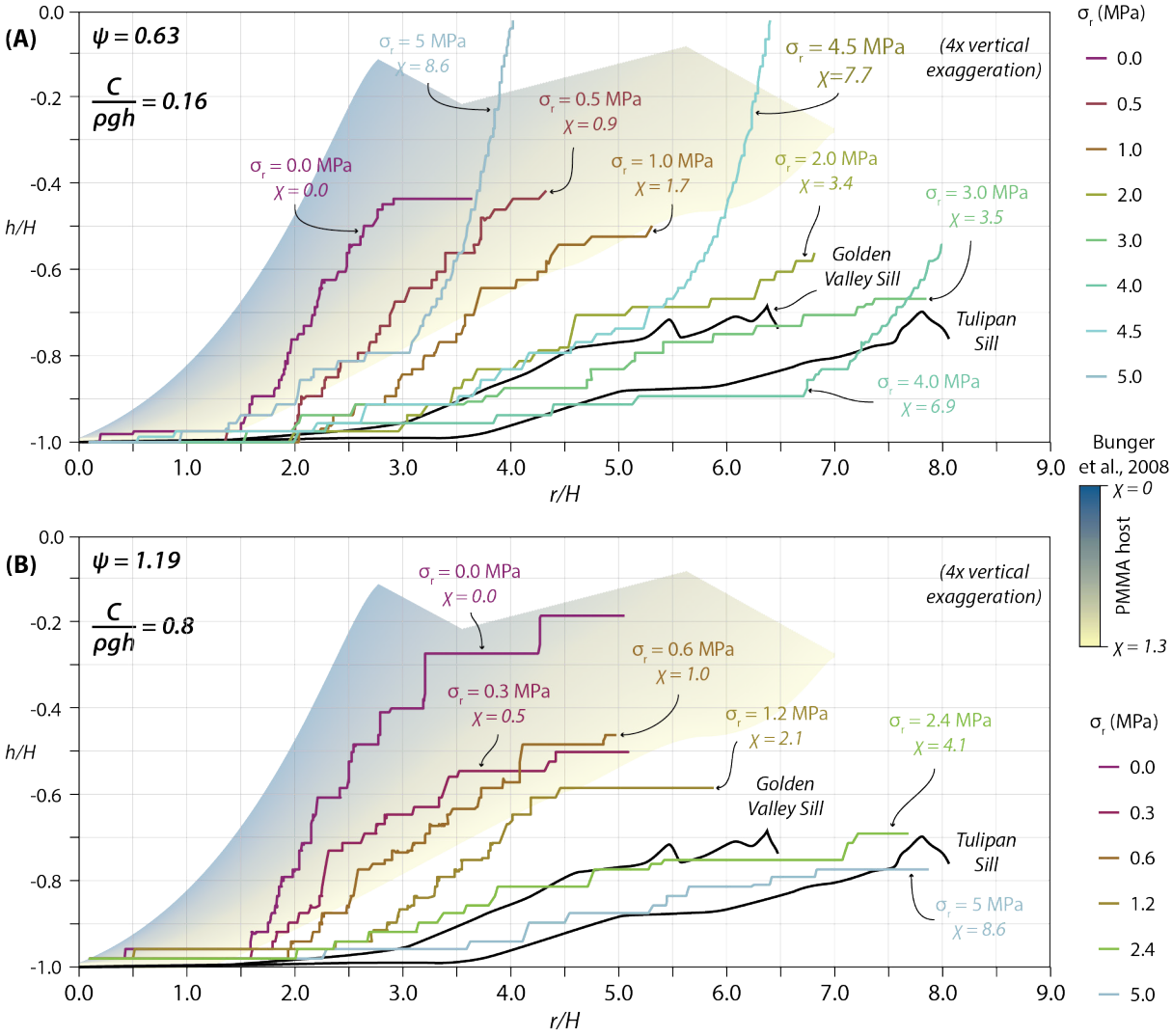

Figure 6. Simplified profiles for simulated sills (this study: vertical plane, radius only) for (**A**) sills seeded at 2 km $\psi = 0.63$ and $\frac{C}{\rho g H} = 0.16$, and (**B**) sills seeded at 1 km $\psi = 1.19$ and $\frac{C}{\rho g H} = 0.8$. Shaded region shows the general field of results for PMMA host analogue models of Bunger et al., (2008).

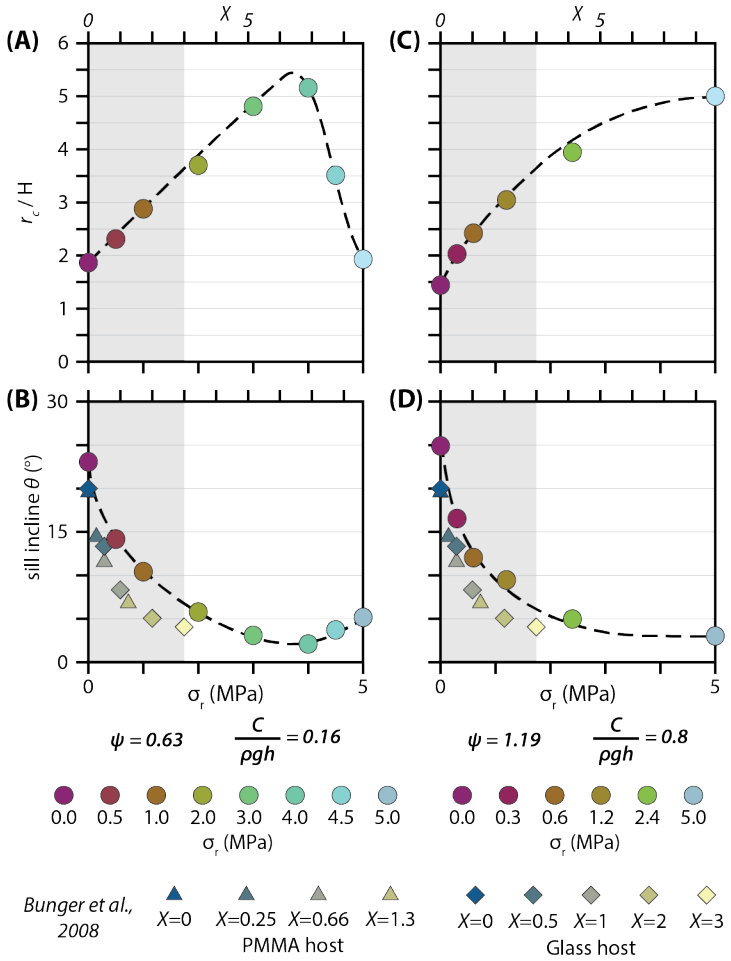

Figure 7. Summary plots of measured critical base length r_c (**A** and **C**) and incline angle θ (**B** and **D**) for simulated sills (this study). Results measured from plots in Bunger et al., (2008) are shown for comparison; grey region shows the range of their χ values. Note that the values for σ_r only correspond to our study.

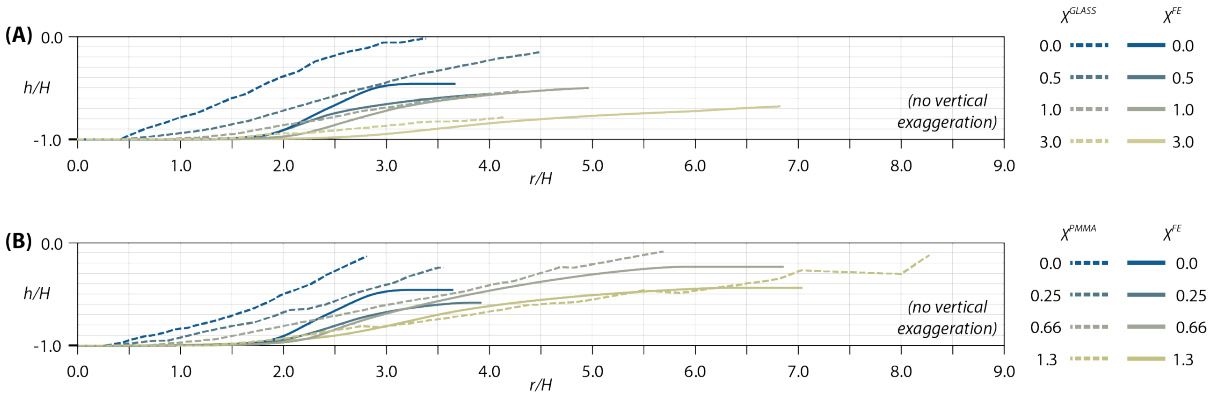

Figure 8. Sill profiles for simulations conducted without lithostatic pressure and buoyancy, and with failure limited to mode I tensile fracture. The range of χ values are chosen for comparison to analogue results from Bunger et al., (2008) for (**A**) glass and (**B**) PMMA hosts.

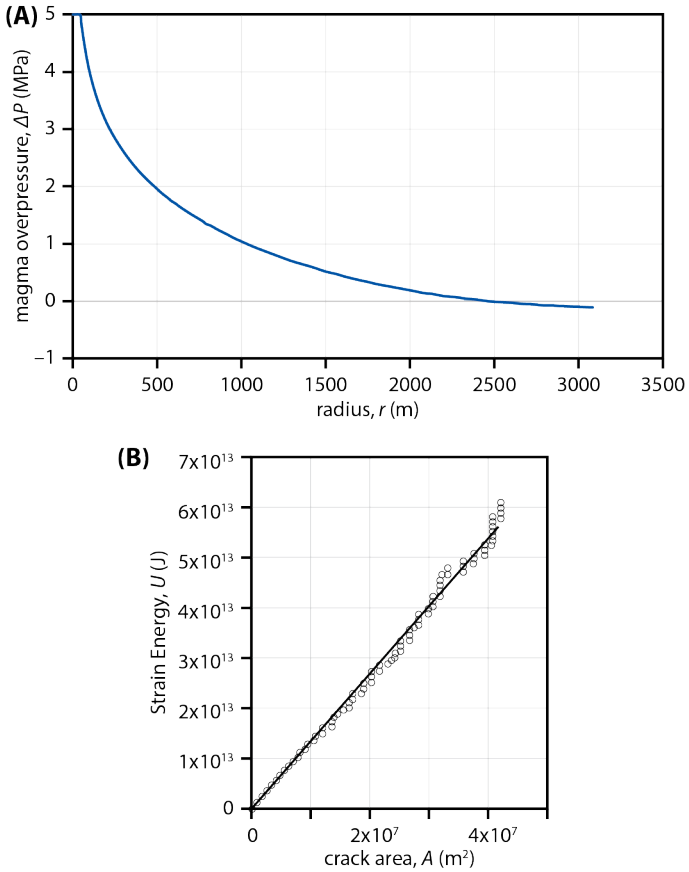

Figure 9. Magma pressure profile within the sill. (**A**) example of the magma pressure profile along the intrusion when it is 3.1km long. (**B**) elastic stored energy U plotted against projected sill area A from the sill propgation simulation with zero tectonic stress.

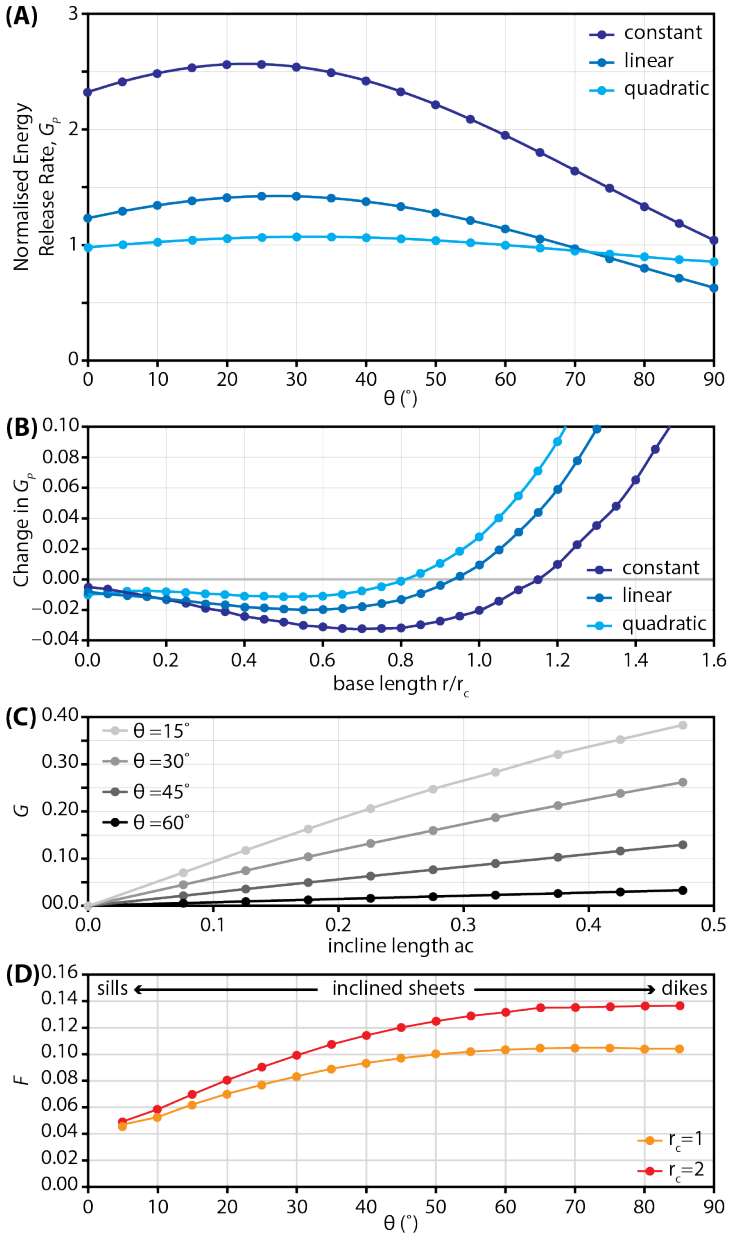

Fig. 10. Calculated energy release rates for the modelled sills. (**A**) Energy release rate for the three different pressure distributions for a sill of base length $a_C = 1.5H$ growing at an inclined angle θ, (**B**) change in energy release rate when a crack changes from growing horizontally to an inclined angle of 25° as a function of the flat section length, $\frac{r_C}{H}$, (**C**) normalised energy release rate for cracks of length $r_c = 1.5H$ subject to a remotely applied stress σ_r and no internal pressure, (**D**) the $F(\theta, \frac{r_C}{H})$ function of Equation 21 as a function of incline angle θ for two different sill base lengths.

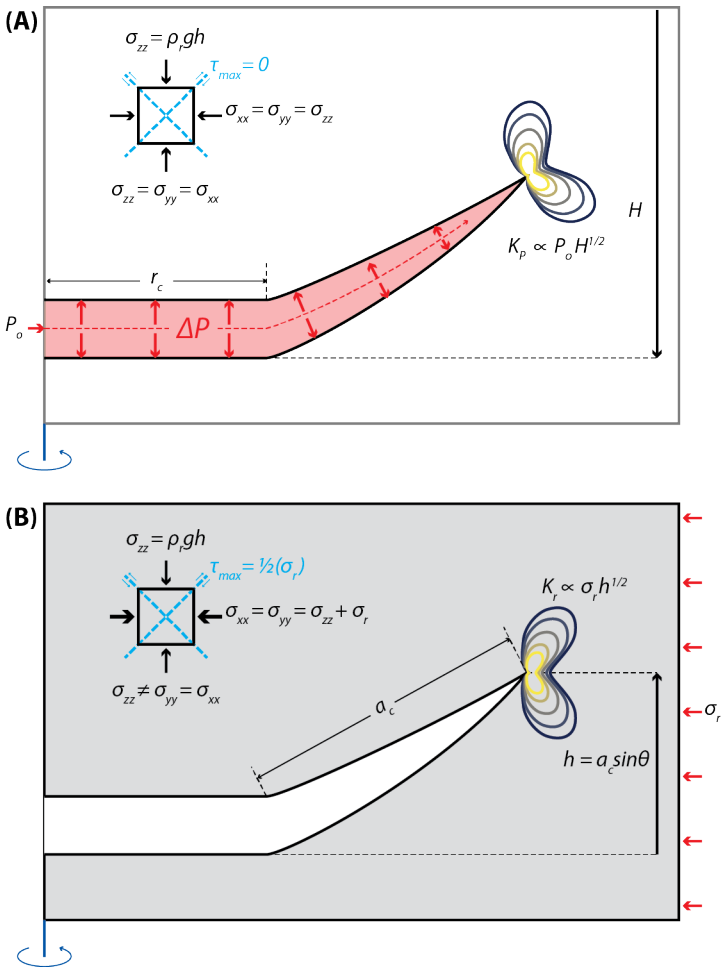

Fig. 11. Schematic illustration of the competing sill tip stress contributions: (**A**) the internal magma pressure has been shown to drive the sill towards the surface at an angle of about 25^o to the horizontal once it has exceeded a length of $r_c \approx H$. This is the dominant stress in driving the sill forwards. (**B**) A compressive applied differential tectonic stress (above lithostatic) acts to reduce the tensile stress at the sill tip caused by the magma pressure. The reduction is minimal in the horizontal plane (as shown) and hence acts to lower the angle of inclination of the sill.

C/ρgh=0.16; ψ=0.63; H=2 km					
σr (Mpa)	*base length (m)*	*rc/H*	*ϑ (°)*	*χ*	*τmax (Mpa)*
0.0	3625	1.81	22.8	0.0	0.00
0.5	4490	2.24	13.7	0.9	0.25
1.0	5667	2.83	9.8	1.7	0.50
2.0	7281	3.64	5.3	3.4	1.00
3.0	9500	4.75	2.6	5.2	1.50
4.0	10240	5.12	1.4	6.9	2.00
4.5	6906	3.45	2.9	7.7	2.25
5.0	3708	1.85	4.7	8.6	2.50
C/ρgh=0.8; ψ=1.19; H= 1km					
σr (Mpa)	*base length (m)*	*rc/H*	*ϑ (°)*	*χ*	*τmax (Mpa)*
0.0	2500	2.50	23.9	0.0	0.00
0.3	3583	3.58	15.4	0.5	0.15
0.6	4333	4.33	11.1	1.0	0.30
1.2	5458	5.46	8.4	2.1	0.60
2.4	7167	7.17	4.0	4.1	1.20
5.0	9083	9.08	1.9	8.6	2.50

Table 1. Summary of sill length scale and geometric parameters for numerical tests with variable σ_r conducted in this study.